JASA Express Letters

MARCH 17 2026

Turbulence-induced noise variability from ray tracing with instantaneous velocity snapshots

Jatinder Goyal ; Frits de Prenter ; Damiano Casalino ; Daniele Ragni

JASA Express Lett. 6, 032801 (2026)
https://doi.org/10.1121/10.0043128

JASA EXPRESS LETTERS ARTICLE asa.scitation.org/journal/jel

Turbulence-induced noise variability from ray tracing with instantaneous velocity snapshots

Jatinder Goyal,[1,2,a] Frits de Prenter,[1,b] Damiano Casalino,[1,3,c] and Daniele Ragni[1,d]
[1]Department of Flow Physics and Technology, Faculty of Aerospace Engineering, Delft University of Technology, Delft, The Netherlands
[2]Suzlon Energy Limited, Hengelo, The Netherlands
[3]Dassault Systèmes Deutschland GmbH, Stuttgart, Germany

Abstract: Turbulence from densely built urban structures alters the acoustic signature of advanced air mobility (AAM) vehicles, complicating prediction of noise impact. Ray tracing, using instantaneous frozen velocity-field snapshots from time-resolved simulations, provides an efficient approach for estimating turbulence-induced acoustic variability. Comparisons of the equivalent sound level (L_{eq}), variability metric ($L_{10} - L_{90}$), and transient sound-level fluctuations show good agreement with a time-resolved reference solution, where discrepancies are mainly near the source and ground. Correlation analysis confirms that dominant temporal variability trends are reproduced at most observer locations, demonstrating that the method provides a reliable and computationally efficient framework for assessing AAM noise in urban environments.

[Editor: Charles C. Church] https://doi.org/10.1121/10.0043128

Received: 19 December 2025 **Accepted:** 6 March 2026 **Published Online:** 17 March 2026

1. Introduction

Noise from advanced air mobility (AAM) vehicles in urban environments is influenced not only by source characteristics but also by unsteady atmospheric and building-induced turbulence along the propagation path. Whereas prior studies have characterized dominant AAM noise sources,[1–3] recent assessments emphasize that propagation effects in complex urban settings must also be addressed.[4] Many existing approaches rely on quasi-steady propagation models based on time-averaged atmospheric profiles.[5–7] However, previous studies have shown that turbulence and refraction can significantly modify transmission loss and shadow-zone behavior, thereby affecting predicted sound levels.[8–12]

Although fully wave-resolved simulations can capture these effects,[13] their computational cost becomes prohibitive for realistic urban domains as a result of the separation between turbulent and acoustic time scales and the large spatial extent required for propagation. This paper proposes a computationally efficient hybrid framework in which statistically representative turbulent flow fields are first obtained (experimentally or computationally), and acoustic ray tracing is then performed on instantaneous velocity snapshots using a frozen-flow assumption to quantify turbulence-induced noise variability.

A key advantage of the approach is the reusability of the given turbulent flow-field dataset for assessing multiple source locations, source strengths, frequencies, or trajectories within the same environment, provided the acoustic source does not significantly alter the background turbulence [a reasonable assumption for most current electric vertical take-off and landing (eVTOL) designs]. Because only the dominant turbulence scales must be resolved, the proposed framework substantially reduces computational cost compared to fully coupled wave-resolved aeroacoustic simulations while retaining physically meaningful variability trends.

To demonstrate the methodology, the acoustic source is modeled as a compact vertical dipole at 100 Hz, representative of tonal components reported for several AAM and eVTOL platforms.[14–19] For validation, the ray-tracing predictions are compared against a high-fidelity lattice-Boltzmann very large-eddy simulations (LB-VLES) simulation that resolves acoustic wave propagation and provides a three-dimensional wave-based reference solution. In this study, only the tonal component is considered; extension to broadband noise is left for future work.

Although turbulence is not the sole driver of AAM noise variability, operational factors, such as thrust modulation, rotor-speed variation, and gust response, can also introduce significant fluctuations.[17,20–23] Reported source-related variations can reach up to approximately 5 dB under gust loading and rotor-speed changes, whereas prior investigations of turbulence-

[a]Corresponding author: j.goyal@tudelft.nl
[b]Email: f.deprenter@tudelft.nl
[c]Email: d.casalino@tudelft.nl
[d]Email: d.ragni@tudelft.nl

induced variability in building wakes[24] indicate fluctuations on the order of 3 dB at certain observer locations. These comparable magnitudes suggest that propagation-induced variability caused by urban turbulence can be of the same order as source-induced effects and, therefore, warrants explicit consideration. The present study isolates propagation-related effects as a necessary step toward integrated modeling frameworks that account for source and propagation mechanisms.

2. Methodology

This section describes the building and acoustic source configuration, followed by a brief description of the LB-VLES simulations used to generate the turbulent flow field and wave-based reference solution, and last, the ray-tracing methodology. Full details of the LB-VLES setup are provided in the companion paper.[24]

2.1 Building and acoustic source specifications

The building geometry, inspired by the Aerospace faculty building of Delft University of Technology, represents a typical mid-rise urban structure.[25,26] Its dimensions are 50 m (H) in height, 10 m ($0.2H$) in the streamwise direction, and 20 m ($0.4H$) in depth. The upstream face is located 200 m downstream of the inlet to ensure minimal influence on the inlet boundary (see Fig. 1).

The acoustic source is modeled as a compact 0.5 m cube located 100 m downstream of the building's front face and 100 m above the ground (i.e., 50 m above the roof; Fig. 1). A sinusoidal wall-normal velocity of amplitude 2 m/s at 100 Hz is imposed on the horizontal faces, generating a dipole-type source representative of AAM rotor noise.[14–19] The resulting source produces a root-mean-square pressure of 17.3 Pa when averaged over a spherical surface of 1 m radius.

2.2 LB-VLES simulation setup

LB-VLES simulations are performed using SIMULIA® PowerFLOW 6-2021-R6, a commercially available solver (Dassault Systèmes SIMULIA, Johnston, RI). This modeling approach has been previously validated for AAM aeroacoustics.[27–33] The computational domain (Fig. 1) spans $28H \times 20H \times 18H$ (streamwise, vertical, and spanwise) and consists of seven variable-resolution regions, with cell volume increasing by a factor of 8 between successive levels. The finest region surrounds the acoustic source and resolves up to five wavelengths in all directions at 100 Hz. This region is embedded within the primary region of interest variable resolution (VR6), which spans 400 m $\times$ 150 m $\times$ 50 m (Fig. 1). All analyses presented in this paper are conducted within the VR6 region. The surrounding coarser regions serve as buffer zones to minimize boundary reflections.

A logarithmic wind profile representative of urban atmospheric conditions[34] is prescribed at the inlet, defined by $U_x(Y) = (u_\star/\kappa)\log_{10}(Y/Y_0 + 1)$, where $u_\star = 1.23$ m/s, $\kappa = 0.41$, and $Y_0 = 0.1$ m. This yields mean wind speeds of approximately 8 m/s at rooftop height ($Y = H$) and 9 m/s at $Y = 2H$. The ground and building surfaces are modeled using a pressure-gradient extended wall model[35,36] and treated acoustically as rigid reflectors. A pressure outlet is applied downstream, with pressure far-field conditions on the lateral and top boundaries.

Flowfield and reference dataset. The proposed framework requires only statistically representative turbulent flow fields and does not rely on acoustically resolved propagation simulations. However, a wave-based reference solution is needed for validation. Accordingly, two LB-VLES datasets are employed: (i) a coarse-resolution simulation capturing building-wake dynamics only, and (ii) a fine-resolution simulation that explicitly resolves acoustic wave propagation. The corresponding computational costs are summarized in Table 1.

The coarse simulation uses a finest voxel size of 0.5 m and requires approximately 2.4 central processing unit (CPU)-hours per second of physical time, totaling about 2400 CPU-hours for a 1000 s simulation.[24] The final 70 s of this dataset are used for the present analysis.

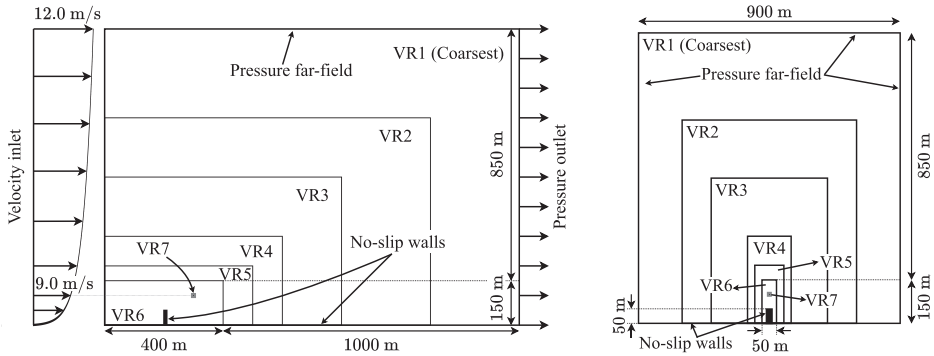

(a) XY plane (b) YZ plane

Fig. 1. Overview of the computational domain and region of interest.

Table 1. Computational cost for the LB-VLES simulations.

Simulation	Simulation duration (s)	Finest voxel size (m)	Time step (s)	Equivalent fine cells	CPU hours/ physical second (h/s)	Total CPU hours (h)
Coarse (flow field only)	1000	0.500	8.019×10^{-4}	1 866 268	2.4	2400
Fine (validation reference)	70	0.086	1.376×10^{-4}	358 459 777	1634.0	114 380

The fine simulation uses a voxel size of 0.086 m (approximately 40 voxels per wavelength in VR7). For a canonical 100 Hz plane wave propagation in a quiescent rectangular domain with 20 voxels per wavelength (representative of the VR6 resolution), the effective decay rate is ≈0.035 dB/m (which is of the same order as that reported in the literature[37]), representing an upper bound that includes numerical and physical damping. This resolution requires 1634 CPU-hours per second of physical time, nearly 680 times higher than that for the coarse simulation. Consequently, the fine simulation is limited to 70 s in total, with 40 s retained for analysis, and initialized from the converged coarse solution to accelerate wake development.

Post-processing. Pressure data are extracted on a 5 m grid in the mid-plane ($Z = 0$) of the VR6 region for subsequent analysis. Signals are bandpass filtered in the [90,110] Hz range to isolate the acoustic component and segmented into 0.02 s windows (two acoustic cycles) with 50% overlap to compute short-time p_{rms}. This window length approximates instantaneous acoustic fields that are consistent with the frozen-flow assumption used in ray tracing.

2.3 Ray-tracing setup

Ray tracing is performed using the ray acoustics interface in COMSOL Multiphysics 6.2 COMSOL (COMSOL AB, Stockholm, Sweden) in the mid-plane ($Z = 0$) of the VR6 region (400 m × 150 m), as shown in Fig. 1(a). A two-dimensional formulation is adopted for this proof-of-concept study, whereas the underlying turbulent velocity field remains fully three-dimensional. This choice is motivated by the availability of archived mid-plane velocity snapshots and the relatively small spanwise velocity fluctuations (<3 m/s) compared to the streamwise and vertical components. In addition, the validation of two-dimensional ray-tracing predictions against a fully three-dimensional wave-based LB-VLES solution provides a conservative assessment of accuracy. Extension to three-dimensional ray tracing is straightforward and requires only volumetric velocity snapshots and, for this reason, is omitted in the paper.

The acoustic source is modeled as a 100 Hz point source with spherical spreading and dipole directivity such that the radiated acoustic power per unit solid angle follows a $\sin^2(\theta)$ dependence, corresponding to the classical $\sin(\theta)$ dipole pressure-amplitude pattern. Rays launched in the $+Y$ and $-Y$ directions are assigned initial phases of 0° and180°, respectively. The source power is set to 1 W/m and subsequently calibrated in the post-processing phase to match the LB-VLES source strength under no-convection conditions.

Instantaneous LB-VLES velocity snapshots are interpolated onto the COMSOL mesh and treated as frozen background fields. The snapshot sampling interval for the ray-tracing calculations is selected based on characteristic turbulence time scales, as quantified by velocity decorrelation times obtained from the LB-VLES flow solution (refer to Sec. 3.1). The mesh resolution ranges between $\lambda/20$ and $\lambda/10$, with a constant background sound speed of 343 m/s. A total of 10 000 rays are launched per snapshot. Ground and building surfaces are modeled as specular reflectors; all other boundaries absorb rays. No atmospheric attenuation is modeled for simplicity (expected to be negligible for the present configuration). Rays are advanced with a 0.5 ms time step until they reach the domain boundaries.

For post-processing, ray positions (q_x, q_y), p_{rms}, phase (ϕ), and reflection counts are extracted from COMSOL and processed in MATLAB (The MathWorks, Inc., Natick, MA). Because the ray-tracing computation is two-dimensional, p_{rms} values are corrected for three-dimensional spreading by dividing by $\sqrt{r}$,[38,39] where r denotes the propagation distance. Subsequently, the ray data are grouped by reflection count. The complex pressure for each group is then independently interpolated onto a 5 m grid and coherently summed to compute the final p_{rms} field for each velocity snapshot.

3. Results

First, this section evaluates turbulence and acoustic time scales to assess the validity of the frozen-flow assumption used in ray tracing. Then, noise variability is examined through statistical metrics and transient signals at representative probe locations.

3.1 Turbulence and sound propagation time scales

The temporal spacing of velocity snapshots for ray tracing is determined from the velocity decorrelation time, defined as the lag $\tau_{R=1/e}$ at which the autocorrelation function falls below $1/e$ [Fig. 2(a)]. To assess the frozen-flow assumption, the ratio $\tau_{R=1/e}/t_{\mathrm{sound}}$ is also evaluated [Fig. 2(b)], where t_{sound} is the acoustic travel time from the source to each spatial location, assuming a constant sound speed of 343 m/s.

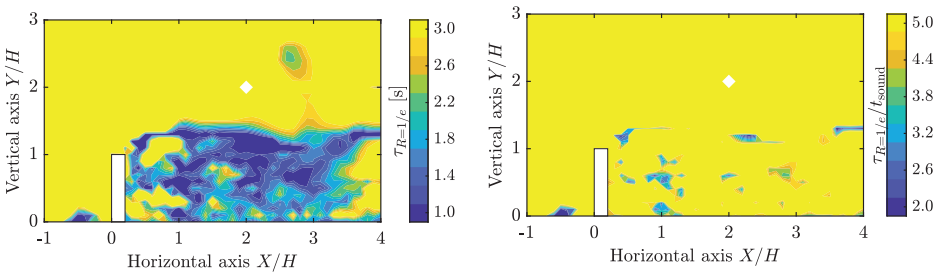

(a) Velocity decorrelation time ($\tau_{R=1/e}$)

(b) Ratio of velocity decorrelation time to the acoustic travel time ($\tau_{R=1/e}/t_{\text{sound}}$)

Fig. 2. Velocity decorrelation analysis and assessment of the frozen-turbulence assumption for ray tracing.

Across most of the building wake, decorrelation times are 1–2 s [Fig. 2(a)]. Shorter times occur within the turbulent wake, where vortex shedding and shear-layer instabilities accelerate the breakdown of coherent structures, whereas longer values appear in weakly disturbed regions outside the wake and near the building. Upstream of the building, a horseshoe vortex forms near the ground at $X/H \approx -0.5$, producing locally reduced decorrelation times.

Based on these time scales, velocity snapshots are sampled every 0.5 s for ray tracing using the fine-resolution simulation, enabling reconstruction of sound-level time histories over the 40 s analysis window, whereas a coarser temporal sampling of every 1 s over a 70 s window, based on the coarse-resolution flow field, is used for statistical analyses. Given dominant velocity decorrelation times of 1–2 s, this reduced sampling frequency remains sufficient to obtain statistically converged estimates of equivalent continuous sound level and temporal noise variability. However, because the velocity field is only captured at discrete 0.5 s intervals, eddies evolving on time scales shorter than 1 s cannot be properly resolved (Nyquist criterion) and also violate the frozen-turbulence assumption underlying the ray-tracing approach. To mitigate aliasing from these unresolved small-scale structures, the acoustic energy (p^2_{rms}) time series obtained from ray tracing are filtered using a moving-average window whose length corresponds to the local velocity decorrelation time ($\tau_{R=1/e}$). This filtering suppresses unresolved high-frequency fluctuations while retaining variability associated with larger turbulence structures. All subsequent statistical metrics and transient signals are computed from the filtered signals.

The ratio $\tau_{R=1/e}/t_{\text{sound}}$ exceeds five throughout most of the domain and remains above five even within the wake, except in localized regions [Fig. 2(b)]. These results indicate that acoustic propagation occurs on time scales much shorter than turbulence evolution, supporting the validity of the frozen-flow assumption for the present ray-tracing analysis.

3.2 Noise variability

Noise variability predicted by ray tracing with frozen flow fields is evaluated by comparison with the LB-VLES reference solution. Fine- and coarse-resolution flow fields are used for ray tracing to assess whether computationally inexpensive turbulence data are sufficient to reproduce statistical noise-variability metrics. Transient sound-level signals are then examined using ray tracing based on the fine-resolution flow field and compared against the LB-VLES reference at representative probe locations.

Statistics. The equivalent continuous sound level, L_{eq}, is computed from the ensemble of N samples as $L_{\text{eq}} = 10\log_{10}((1/N)\sum_{i=1}^{N} p^2_{\text{rms},i}/p^2_{\text{ref}})$. To assess temporal variability, exceedance levels L_{10} and L_{90} are extracted from the distribution of instantaneous sound pressure level (SPL) values (L_i), where $L_i = 20\log_{10}(p_{\text{rms},i}/p_{\text{ref}})$. This variability is quantified through the inter-percentile range ($L_{10} - L_{90}$).

The resulting contours of L_{eq} and $L_{10} - L_{90}$ are displayed in Fig. 3 for (i) the LB-VLES reference, (ii) ray tracing based on the fine-resolution flow field, and (iii) ray tracing based on the coarse-resolution flow field. In the full-wave LB-VLES solution, the building casts a clear acoustic shadow upstream; however, finite SPLs and non-negligible variability are still observed in this region as a result of diffraction at the building edges and scattering by turbulent structures. In contrast, geometrical ray tracing yields no solution in this region because neither direct nor reflected rays reach it.[40,41] The plots are, therefore, overlaid with limiting rays, indicating the upstream shadow region (black dashed line) and the farthest ground-reflected ray (red dashed lines). Key features consistently observed across the fields are annotated with letters (a)–(j) for L_{eq} and (a)–(l) for $L_{10} - L_{90}$].

The L_{eq} fields show similar acoustic patterns for both methods [Figs. 3(a) and 3(b)]. Near the building top edge (a), the contour shapes are comparable, although ray tracing predicts slightly higher levels. Above the building, alternating high- and low-level fringes [(b), (c)] appear in both methods due to interference between direct and ground-reflected waves, with somewhat stronger levels predicted by ray tracing. Close to the source [(d)–(f)], both methods yield similar L_{eq} values and contour shapes. Directly below the source, interference between the direct and ground-reflected paths produces

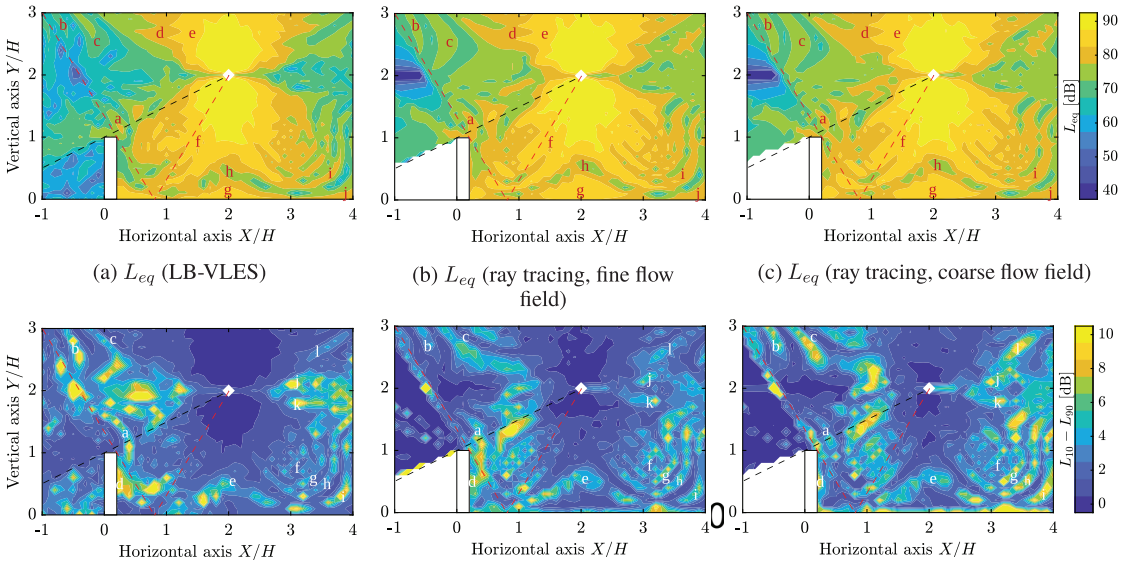

(a) L_{eq} (LB-VLES) (b) L_{eq} (ray tracing, fine flow field) (c) L_{eq} (ray tracing, coarse flow field)

(d) $L_{10} - L_{90}$ (LB-VLES) (e) $L_{10} - L_{90}$ (ray tracing, fine flow field) (f) $L_{10} - L_{90}$ (ray tracing, coarse flow field)

Fig. 3. Comparison of equivalent sound levels (L_{eq}) and sound-level variability ($L_{10} - L_{90}$) predicted by LB-VLES and ray tracing using fine- and coarse-resolution flow fields.

alternating high (g) and low (h) regions. Although these features are present in both approaches, ray tracing predicts a broader high-level zone (g) with a slight upward shift of the adjacent low-level region (h). Further downstream, interference fringes [(i), (j)] exhibit consistent spatial trends in both methods. Ray tracing based on the coarse-resolution flow field [Fig. 3(c)] reproduces these trends nearly identically, demonstrating that coarse flow fields are sufficient to capture the L_{eq} distribution.

The $L_{10} - L_{90}$ fields [Figs. 3(d) and 3(e)] exhibit close agreement between ray tracing and the LB-VLES reference. All key features [(a)–(l)] are reproduced with similar spatial structure, although some differences in variability magnitude are observed. Ray tracing based on the fine-resolution flow field tends to underestimate variability, particularly outside the wake region. This behavior is attributed to the larger velocity decorrelation times in these regions [Fig. 2(a)], which result in wider smoothing windows and, therefore, reduced fluctuation levels. Nevertheless, the coarse-flow-field results reproduce most of the spatial features present in the LB-VLES reference solution [Fig. 3(f)], indicating that the variability metric $L_{10} - L_{90}$ can be estimated using computationally inexpensive coarse-flow-field datasets.

Transient signal. Transient sound-level signals are analyzed to evaluate whether ray tracing captures the temporal evolution of turbulence-induced noise variability, where time histories are expressed as $(L_i - L_{eq})$, where L_i is the instantaneous sound level. This analysis uses ray tracing based on the fine-resolution flow field only because the coarse simulation is not temporally synchronized with the LB-VLES reference and is, therefore, unsuitable for instantaneous comparisons. The analysis is performed at nine probe locations formed by combining three streamwise positions ($X/H = 0.6$, 2.0, and 3.5, which refer to near the building, aligned with the source, and downstream, respectively) and three vertical positions ($Y/H = 0.2$, 1.0, 2.5, which refer to close to the ground, within the shear layer, and above the source, respectively). In Fig. 4, the plots are arranged with streamwise position increasing from left to right and vertical position decreasing from top to bottom; each plot displays the ray-tracing signal (solid line) alongside the LB-VLES reference (dotted line). Agreement between the two signals is quantified using the Pearson correlation coefficient.

At $Y/H = 2.5$ (top row), the probe upstream of the source ($X/H = 0.6$) shows good agreement ($r = 0.66$), where the ray-tracing signal follows the overall LB-VLES trend, albeit with higher amplitude. Directly above the source ($X/H = 2.0$), the correlation drops to $r \approx 0.00$ because the observer lies within the acoustic near field (less than eight acoustic wavelengths), where geometrical ray tracing cannot accurately represent wave effects.[40] Further downstream ($X/H = 3.5$), moderate agreement is recovered ($r = 0.46$), indicating that the dominant variability trends are reproduced.

Within the shear-layer region ($Y/H = 1.0$, middle row), a very good agreement is observed at $X/H = 0.6$ ($r = 0.89$), indicating that the ray-tracing solution closely reproduces turbulence-driven noise fluctuations. Downstream locations also show good agreement ($r = 0.64$ at $X/H = 3.5$), whereas at $X/H = 2.0$, the correlation becomes negative ($r = -0.40$) as a result of a phase shift between the two signals. This shift arises from small differences in predicted interference patterns associated with the expanded high-SPL region [(g) in Fig. 3(b)] in the ray-tracing solution.

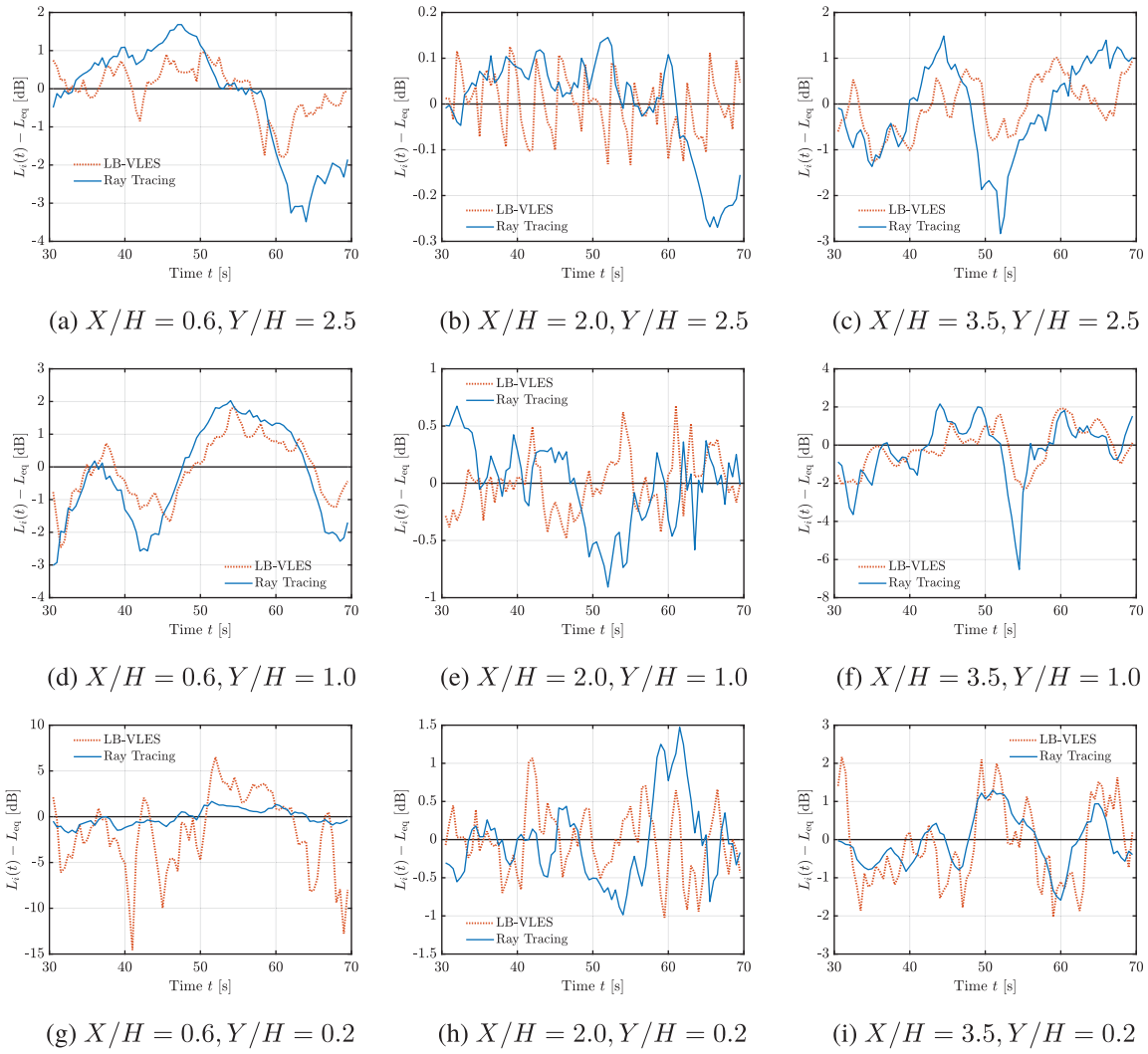

(a) $X/H = 0.6, Y/H = 2.5$ (b) $X/H = 2.0, Y/H = 2.5$ (c) $X/H = 3.5, Y/H = 2.5$

(d) $X/H = 0.6, Y/H = 1.0$ (e) $X/H = 2.0, Y/H = 1.0$ (f) $X/H = 3.5, Y/H = 1.0$

(g) $X/H = 0.6, Y/H = 0.2$ (h) $X/H = 2.0, Y/H = 0.2$ (i) $X/H = 3.5, Y/H = 0.2$

Fig. 4. Temporal evolution of sound-level fluctuations ($L_i - L_{eq}$) at selected probe locations, comparing LB-VLES reference results with ray-tracing predictions based on fine-resolution frozen flow-field snapshots.

Near the ground ($Y/H = 0.2$, bottom row), good agreement is observed at $X/H = 0.6$ ($r = 0.65$), and $X/H = 3.5$ ($r = 0.64$). However, ray tracing significantly underestimates the variability amplitude at $X/H = 0.6$ due to the shift of the interference pattern. At $X/H = 2.0$, the correlation remains weak ($r = -0.24$), reflecting phase differences caused by shifts in constructive and destructive interference patterns close to the ground.

Overall, the correlation analysis indicates that ray tracing reproduces the dominant temporal trends of turbulence-induced acoustic variability at most observer locations ($r = 0.46$–0.89), where discrepancies are primarily near the source line ($X/H = 2$) attributed to near-field effects and interference-pattern shifts.

4. Concluding remarks

This study demonstrates that acoustic ray tracing based on instantaneous frozen flow-field snapshots provides an efficient and reliable approach for estimating turbulence-induced noise variability in urban air mobility scenarios. Analysis of turbulence decorrelation times relative to acoustic propagation times confirms that for the present configuration, the frozen-flow assumption is valid throughout most of the building wake.

Comparison with a fully resolved, three-dimensional wave-based LB-VLES reference solution shows that acoustic ray tracing combined with frozen turbulent flow-field snapshots reliably reproduces turbulence-induced noise variability. The method captures the spatial distributions of the equivalent sound level (L_{eq}) and variability metric ($L_{10} - L_{90}$) with good fidelity, and these statistical metrics are shown to be insensitive to flow-field resolution. This indicates that computationally inexpensive coarse simulations are sufficient provided that the dominant turbulence scales are resolved.

Analysis of transient sound-level fluctuations further shows that the dominant temporal trends driven by large-scale turbulence are reproduced, with moderate to strong correlation between ray-tracing predictions and LB-VLES reference at most observer locations.

Overall, the proposed hybrid framework replaces prohibitively expensive fully coupled aeroacoustic simulations with a reusable and significantly cheaper turbulent flow-field dataset generation step followed by ray-tracing calculations, making it a practical and scalable tool for assessing turbulence-induced contributions to urban noise propagation.

Acknowledgments

The research leading to these results is part of the eVTOLUTION project. This project has received funding from the European Union's Horizon Europe programme under Grant No. 101138209. This work made use of the Dutch national e-infrastructure with the support of the SURF Cooperative using Grant No. EINF-9226.

Author Declarations

Conflict of Interest

The authors have no conflicts to disclose.

Data Availability

The data that support the findings of this study are available from the corresponding author upon reasonable request.

References

[1]C. E. Tinney and J. Sirohi, "Multirotor drone noise at static thrust," AIAA J. **56**(7), 2816–2826 (2018).
[2]H. Lee and D.-J. Lee, "Rotor interactional effects on aerodynamic and noise characteristics of a small multirotor unmanned aerial vehicle," Phys. Fluids **32**(4), 047107 (2020).
[3]R. S. McKay, M. J. Kingan, S. T. Go, and R. Jung, "Experimental and analytical investigation of contra-rotating multi-rotor uav propeller noise," Appl. Acoust. **177**, 107850 (2021).
[4]S. A. Rizzi, D. L. Huff, D. D. Boyd, P. Bent, B. S. Henderson, K. A. Pascioni, D. C. Sargent, D. L. Josephson, M. Marsan, H. B. He, and R. Snider, "Urban air mobility noise: Current practice, gaps, and recommendations," NASA/TP-20205007433, NASA, Washington, DC (2020).
[5]H. Bian, Q. Tan, S. Zhong, and X. Zhang, "Assessment of UAM and drone noise impact on the environment based on virtual flights," Aerosp. Sci. Technol. **118**, 106996 (2021).
[6]F. Yunus, D. Casalino, F. Avallone, and D. Ragni, "Efficient prediction of urban air mobility noise in a vertiport environment," Aerosp. Sci. Technol. **139**, 108410 (2023).
[7]C. Wu and S. Redonnet, "Aircraft noise impact prediction with incorporation of meteorological effects," Transp. Res. Part D: Transp. Environ. **125**, 103945 (2023).
[8]T. Van Renterghem, K. V. Horoshenkov, J. A. Parry, and D. P. Williams, "Statistical analysis of sound level predictions in refracting and turbulent atmospheres," Appl. Acoust. **185**, 108426 (2022).
[9]D. K. Wilson, C. L. Pettit, V. E. Ostashev, and M. J. Kamrath, "Signal power distributions for simulated outdoor sound propagation in varying refractive conditions," J. Acoust. Soc. Am. **151**(6), 3895–3906 (2022).
[10]E. Salze, S. Ollivier, E. Jondeau, and P. Blanc-Benon, "Laboratory-scale experiment to study *n*-wave propagation into a shadow zone with turbulence," AIAA J. **63**(11), 4662–4670 (2025).
[11]Y. W. Lam, "An analytical model for turbulence scattered rays in the shadow zone for outdoor sound propagation calculation," J. Acoust. Soc. Am. **125**(3), 1340–1350 (2009).
[12]V. E. Ostashev and D. K. Wilson, *Acoustics in Moving Inhomogeneous Media*, 2nd ed. (CRC Press, Boca Raton, FL, 2015).
[13]D. Casalino, M. Barbarino, and A. Visingardi, "Simulation of helicopter community noise in complex urban geometry," AIAA J. **49**(8), 1614–1624 (2011).
[14]D. Perry, "Blade release due to manufacturing defect doomed VX4 prototype, says UK AAIB," (2024), available at https://www.flightglobal.com/aerospace/blade-release-due-to-manufacturing-defect-doomed-vx4-prototype-says-uk-aaib/158122.article (Last viewed 05-22-2025).
[15]O. Johnson, "Cityairbus set for first flight in March" (2019), available at https://verticalmag.com/news/cityairbus-set-for-first-flight-in-march/ (Last viewed 05-22-2025).
[16]G. Warwick, "NASA's electric-propulsion wing test helps shape next X-plane" (2015), available at https://aviationweek.com/aerospace/nasas-electric-propulsion-wing-test-helps-shape-next-x-plane (Last viewed 05-22-2025).
[17]K. A. Pascioni, M. E. Watts, M. Houston, A. Lind, J. H. Stephenson, and J. Bain, "Acoustic flight test of the joby aviation advanced air mobility prototype vehicle," in *28th AIAA/CEAS Aeroacoustics 2022 Conference*, Southampton, UK (June 14–17) (AIAA, Reston, VA, 2022), p. 3036.
[18]A. Thai and A. S. Engineer, "Flyover noise computations of the joby aviation aircraft," Horizon **270**(300), 60 (2023).
[19]K. A. Pascioni, A. D. Thai, and J. J. Bain, "Propeller source noise separation from flight test measurements of the joby aviation aircraft," in *30th AIAA/CEAS Aeroacoustics Conference*, Rome, Italy (June 4–7) (AIAA, Reston, VA, 2024), p. 3231.
[20]Y. Li, Z. Ma, R. Qu, Q. Tan, S. Zhong, P. Zhou, and X. Zhang, "Effect of rotation speed fluctuation on rotor noise generation: A numerical and experimental study," J. Sound Vib. **595**, 118717 (2025).
[21]Y. Li, X. Li, H. Wu, P. Zhou, X. Zhang, and S. Zhong, "Experimental and numerical investigations on rotor noise in axial descending flight," Phys. Rev. Fluids **8**, 094803 (2023).
[22]J. Ko, Y. Kim, J. Jeong, and S. Lee, "Prediction-based psychoacoustic analysis of multirotor noise under gusty wind conditions," J. Acoust. Soc. Am. **154**(5), 3004–3018 (2023).

[23]V. Voropayev, M. Marques, A. Maleki, S. Grace, A. S. Lyrintzis, R. R. Mankbadi, and V. V. Golubev, "High-fidelity simulations of vertiport gust effects on evtol rotor noise," in *AIAA Aviation Forum and ASCEND*, Las Vegas, NV (July 21–25) (AIAA, Reston, VA, 2025), p. 3001.
[24]J. Goyal, F. de Prenter, D. Ragni, and D. Casalino, "Impact of building wake turbulence on the noise footprint of a dipole source," J. Acoust. Soc. Am. **159**(2), 1304–1315 (2026).
[25]K. Al-Kodmany, *The Vertical City: A Sustainable Development Model* (WIT, Southampton, UK, 2018).
[26]V. Cheng, "Understanding density and high density," in *Designing High-Density Cities for Social and Environmental Sustainability*, edited by E. Ng (Earthscan, London, UK, 2010), pp. 3–17.
[27]E. Grande, S. Shubham, F. Avallone, D. Ragni, and D. Casalino, "Computational aeroacoustic study of co-rotating rotors in hover," Aerosp. Sci. Technol. **153**, 109381 (2024).
[28]D. Casalino, G. Romani, L. M. Pii, and R. Colombo, "Flow confinement effects on sUAS rotor noise," Aerosp. Sci. Technol. **143**, 108756 (2023).
[29]D. Casalino, G. Romani, R. Zhang, and H. Chen, "Lattice-Boltzmann calculations of rotor aeroacoustics in transitional boundary layer regime," Aerosp. Sci. Technol. **130**, 107953 (2022).
[30]G. Romani, E. Grande, F. Avallone, D. Ragni, and D. Casalino, "Computational study of flow incidence effects on the aeroacoustics of low blade-tip mach number propellers," Aerosp. Sci. Technol. **120**, 107275 (2022).
[31]G. Romani, E. Grande, F. Avallone, D. Ragni, and D. Casalino, "Performance and noise prediction of low-Reynolds number propellers using the Lattice-Boltzmann method," Aerosp. Sci. Technol. **125**, 107086 (2022).
[32]D. Casalino, W. C. van der Velden, G. Romani, and I. Gonzalez-Martino, "Aeroacoustic analysis of urban air operations using the LB/VLES method," in *25th AIAA/CEAS Aeroacoustics Conference*, Delft, The Netherlands (May 20–23) (AIAA, Reston, VA, 2019), p. 2662.
[33]D. Casalino, W. C. van der Velden, and G. Romani, "Community noise of urban air transportation vehicles," in *AIAA Scitech 2019 Forum*, San Diego, CA (January 7–11) (AIAA, Reston, VA, 2019), p. 1834.
[34]E. Salomons, *Computational Atmospheric Acoustics* (Kluwer Academic, Dordrecht, The Netherlands, 2001), pp. 40–42.
[35]C. M. Teixeira, "Incorporating turbulence models into theL-Boltzmann method," Int. J. Mod. Phys. C **09**(08), 1159–1175 (1998).
[36]D. C. Wilcox, *Turbulence Modelling for CFD*, 3rd ed. (DCW Industries, La Cañada, CA, 2006).
[37]G. Brès, F. Pérot, and D. Freed, "Properties of the Lattice Boltzmann method for acoustics," in *15th AIAA/CEAS Aeroacoustics Conference (30th AIAA Aeroacoustics Conference)*, Miami, FL (May 11–13) (AIAA, Reston, VA, 2009), p. 3395.
[38]D. T. Blackstock, "On plane, spherical, and cylindrical sound waves of finite amplitude in lossless fluids," J. Acoust. Soc. Am. **36**(1), 217–219 (1964).
[39]D. Weston, "Intensity-range relations in oceanographic acoustics," J. Sound Vib. **18**(2), 271–287 (1971).
[40]"The ray acoustics interface" (Comsol Multiphysics 6.2 documentation), available at https://doc.comsol.com/6.2/doc/com.comsol.help.aco/aco_ug_geometrical_aco.11.02.html (Last viewed 9-30-2025).
[41]P. M. Bakker, "Theory of edge diffraction in terms of dynamic ray tracing," Geophys. J. Int. **102**(1), 177–189 (1990).